

Closed-form tidal approximants for binary neutron star gravitational waveforms constructed from high-resolution numerical relativity simulations

Tim Dietrich¹, Sebastiano Bernuzzi^{2,3}, and Wolfgang Tichy⁴

¹*Max Planck Institute for Gravitational Physics (Albert Einstein Institute), Am Mühlenberg 1, Potsdam 14476, Germany*

²*Department of Mathematical, Physical and Computer Sciences, University of Parma, I-43124 Parma, Italy*

³*Istituto Nazionale di Fisica Nucleare, Sezione Milano Bicocca,
gruppo collegato di Parma, I-43124 Parma, Italy and*

⁴*Department of Physics, Florida Atlantic University, Boca Raton, FL 33431 USA*

(Dated: July 6, 2018)

We construct closed-form gravitational waveforms (GWs) with tidal effects for the coalescence of binary neutron stars. The method relies on a new set of eccentricity-reduced and high-resolution numerical relativity (NR) simulations and is composed of three steps. First, tidal contributions to the GW phase are extracted from the time-domain NR data. Second, those contributions are employed to fix high-order coefficients in an effective and resummed post-Newtonian expression. Third, frequency-domain tidal approximants are built using the stationary phase approximation. Our tidal approximants are valid from the low frequencies to the strong-field regime. They can be analytically added to any binary black hole GW model to obtain a binary neutron star waveform, either in the time or in the frequency domain. This work provides simple, flexible, and accurate models ready to be used in both searches and parameter estimation of binary neutron star events.

PACS numbers: 04.25.D-, 04.30.Db, 95.30.Sf, 95.30.Lz, 97.60.Jd

INTRODUCTION

The 2015 detections of gravitational waves (GWs) of merging binary black holes (BBHs) [1, 2] have initiated a new observational era in astronomy and fundamental physics. In the coming years, ground-based advanced interferometers will reach design sensitivity and observe the coalescence and merger of binary neutron stars (BNSs) [3]. These observations will have a unique potential to probe the fundamental physics of NSs and to connect high-energy astrophysical phenomena with their strong-gravity engines. The main examples are the possibility to constrain the equation of state (EOS) of the cold ultradense matter in NS interiors, e.g. [4], and the possibility to show the unequivocal connection between electromagnetic signals, e.g. short gamma ray bursts [5] or kilonovae [6], with the collision of two compact objects.

A key open problem for GW astronomy with BNS sources is the availability of faithful waveform models that capture the strong-gravity and tidally dominated regime of the late-inspiral and merger. State-of-the-art tidal waveform models have been developed in [7, 8] and are based on the effective-one-body (EOB) description of the general-relativistic two-body problem [9, 10]. That approach proved to be very powerful but has also limitations. EOB waveforms cannot be efficiently evaluated, hence they cannot be directly used for GW searches or parameter estimation. Fast representations of EOB can be build using reduced-order-modeling techniques [11], but they require extra efforts and introduce further uncertainties. Additionally, the currently published tidal EOB models neither include spin effects nor are tested against spinning NR simulations [12]. Recent work also showed that the current EOB models are not uniformly

accurate on the binary parameter space that has been simulated in Ref. [13, 14]. Thus, modeling techniques complementary to EOB, see e.g. [15, 16], are needed especially because post-Newtonian (PN) approximants fail towards merger and introduce systematic uncertainties in GW parameter estimation [17–19].

In this work, we construct for the first time closed-form (analytical) approximants to the tidal GW phase directly employing numerical relativity (NR) simulations. Simple time and frequency domain approximants are build from a set of error-controlled BNS merger simulations. Our method is inspired by some ideas used in the modeling of BBH's GWs. In particular, it makes direct use of NR data as in the Phenom approach [20] and employs resummed PN expressions as in the EOB approach.

ECCENTRICITY-REDUCED AND HIGH-RESOLUTION NR SIMULATIONS

For this work, we simulated nine BNS configurations in general relativity. We simulated equal-mass BNSs both irrotational and with spins (anti) aligned to the orbital angular momentum. Three different parameterized EOSs (MS1b, H4, SLy) [21] are employed to span a large range of tidal parameters (see below). The binary gravitational mass is $M = M_A + M_B \sim 2.7$, where A, B label the NSs and M_A is the mass of star A in isolation. Spin magnitudes are in the range $\chi_A = \chi_B \sim [-0.1, +0.15]$, where $\chi_A = S_A/M_A^2$ is the mass-rescaled dimensionless spin. We use the numerical methods implemented in the pseudospectral initial data SGRID code [22] and in the 3+1 adaptive-mesh-refinement evolution BAM code [23]. Key technical points are the use of the Z4c formulation

of general relativity and of a high-order scheme for the hydrodynamics [24, 25]. See [26] for further details. Note that we employ geometric units $G = c = M_\odot = 1$.

These new simulations significantly improve the waveform's quality over previous ones. Low-eccentricity initial data were generated following Ref. [27]; our BNSs have $e \sim 10^{-3}$. Each BNS is evolved using four to five grid resolutions making a total of 37 runs. The NSs are resolved with smallest grid spacings in the range $dx = 0.291 - 0.059$ in each direction. These are the largest BNS simulations performed with the BAM code so far and utilized ~ 25 million CPU hours on various high-performance-computing clusters. Numerical uncertainties are estimated from convergence tests and a detailed error budget has been computed. Our waveforms have maximal errors at merger, accumulated over ~ 12 orbits, of $\sim 0.5 - 1.5$ radians, depending on the particular configuration [26]. The waveforms are publicly available under www.computational-relativity.org; see Refs. [28, 29] for more details.

EXTRACTION OF TIDAL CONTRIBUTIONS

Spin and tidal effects in the phase of the complex GW $h(t) = A(t)e^{-i\phi(t)}$ are parametrized to leading PN order, respectively, by the effective spin

$$\chi_{\text{eff}} = X_A \chi_A + X_B \chi_B - \frac{38}{113} X_A X_B (\chi_A + \chi_B) \quad (1)$$

describing the spin-orbit (SO) interaction [30], and by an effective tidal coupling constant [10, 32]

$$\kappa_{\text{eff}}^T = \frac{2}{13} \left[\left(1 + 12 \frac{X_B}{X_A} \right) \left(\frac{X_A}{C_A} \right)^5 k_2^A + (A \leftrightarrow B) \right], \quad (2)$$

where k_2^A is the quadrupolar Love number describing the static quadrupolar deformation of one body in the gravitoelectric field of the companion, $X_A = M_A/M$, and C_A is the compactness of star A . κ_{eff}^T is defined here for the first time but it based on the expressions for generic mass ratio phasing in [32]. For equal mass systems κ_{eff}^T is identical to the dimensionless tidal coupling constant κ_2^T defined in [10, 41].

In order to separate the tidal phase, we work with the phase as a function of the dimensionless GW frequency $\hat{\omega} = M \partial_t \phi(t)$ and use the PN *ansatz*,

$$\phi(\hat{\omega}) \approx \phi_0(\hat{\omega}) + \phi_{\text{SO}}(\hat{\omega}) + \phi_T(\hat{\omega}), \quad (3)$$

where ϕ_0 denotes the nonspinning black hole (or point particle) phase evolution. The SO contribution is $\phi_{\text{SO}} \propto \chi_{\text{eff}}$ at leading 1.5PN order and it is currently known up to 3.5PN order. For simplicity, we neglect spin-spin interactions; they are subdominant contributions and poorly resolved in our simulations [31]. Tidal contributions

enter the phasing at 5PN. The currently known next-to-leading-order PN expression of the tidal contribution (TaylorT2 approximant) [19] reads

$$\phi_T^{\text{T2}} = -\kappa_{\text{eff}}^T \frac{c_{\text{Newt}} x^{5/2}}{X_A X_B} (1 + c_1 x), \quad (4)$$

with $x(\hat{\omega}) = (\hat{\omega}/2)^{2/3}$, where $\hat{\omega}/2$ is the orbital frequency, and $c_{\text{Newt}} = -13/8$, $c_1 = 1817/364$ (value for equal mass case). Using Eq. (3) the nonperturbative SO and tidal contributions can be extracted by linearly combining pairs of simulation data with different parameters, as detailed in [12, 26, 31]. The top of Fig. 1 shows the total phase accumulated over simulations. The bottom shows the phase differences divided by the differences in κ_{eff}^T for several simulation pairs [26], denoted by $\Delta\phi_T/\Delta\kappa_{\text{eff}}^T$. According to Eqs. (3) and (4) $\Delta\phi_T/\Delta\kappa_{\text{eff}}^T \approx \phi_T/\kappa_{\text{eff}}^T$. For comparison we also show $\phi_T/\kappa_{\text{eff}}^T$ of our fit and of TaylorT2. We find that the leading-order EOS effect is captured well by κ_{eff}^T and the residual dependency on the EOS, related to multipolar tidal coefficients with $\ell > 2$, is negligible. Most importantly, tidal interactions decouple from spin interactions for the spin values explored by NR data and at level of the NR uncertainties. This fact allows us to construct spinning BNSs using binary black hole baseline waveforms and adding the tidal contribution. Further, Fig. 1 indicates that the TaylorT2 approximant does *not* capture the phase evolution in the strong field region, failing for $\hat{\omega} \gtrsim 0.06$, which is approximately the contact frequency [17].

TIME-DOMAIN TIDAL APPROXIMANT

A closed-form expression for ϕ_T is obtained using the fitting formula

$$\phi_T = -\kappa_{\text{eff}}^T \frac{c_{\text{Newt}} x^{5/2}}{X_A X_B} \times \frac{1 + n_1 x + n_{3/2} x^{3/2} + n_2 x^2 + n_{5/2} x^{5/2} + n_3 x^3}{1 + d_1 x + d_{3/2} x^{3/2}} \quad (5)$$

Demanding that Eq. (5) reproduces Eq. (4) in a low frequency expansion, we set $d_1 = (n_1 - c_1)$. The other coefficients are fit to NR data. Note that for simplicity Eq. (5) does not contain tidal terms corresponding to higher multipoles [32], and the dependency from $X_{A,B}$ of the higher effective PN terms is ignored. This is justified since we seek an effective expression of the phase; the coefficients of the latter could be further improved using more simulations with various mass ratios.

The fit is performed on a dataset spanning the interval $\hat{\omega} \in [0, 0.17]$. Eq. (4) is used for $\hat{\omega} \leq 0.0074$, while the tidal EOB waveforms of [7] are used for $\hat{\omega} \geq [0.0074, 0.04]$. The datasets are connected such that phase differences near the interval boundaries are minimal. We interpolate the data on a grid consisting of

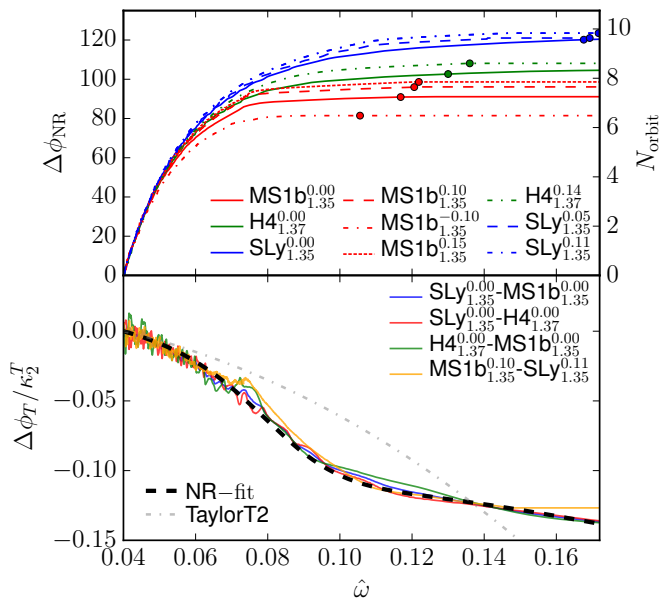


FIG. 1. Phase as a function of the GW frequency from NR simulations. The simulations are labeled as $\text{EOS}_{M,A}^{X,A}$. Top: Total phase / number of cycles accumulated within frequency interval $\hat{\omega} \in [0.04, 0.17]$ for different BNSs. Markers indicate the merger (peak of the GW’s amplitude) of the particular simulation for the highest revolved simulation. Bottom: Pair-wise phase differences equivalent to the tidal phase $\phi_T/\kappa_{\text{eff}}^T$; note the spin independence.

10000, 5000, 500 points in the three intervals, respectively. Although the final fit depends only weakly on the exact number of points of the interpolating grid, using more points at lower frequencies helps constraining the fit in that regime. Our approximant is defined by Eq. (5) with the fitting coefficients $(n_1, n_{3/2}, n_2, n_{5/2}, n_3) = (-17.941, 57.983, -298.876, 964.192, -936.844)$, and $d_{3/2} = 43.446$.

A time-domain approximant of a BNS configuration is computed by prescribing κ_{eff}^T and adding Eq. (5) to a BBH baseline, i.e. to ϕ_0 . To construct a generic spin-aligned BNS configurations with spin χ_{eff} we use a BBH waveform that includes already the spin contribution, i.e. use as baseline the GW phase of a BBH setup which has the same dimensionless spin as the BNS configuration which we are going to model. The time-domain phasing is then calculated by numerically integrating $t = \int d\phi/\hat{\omega}(\phi)$ in order to obtain a parametric representation of the tidal phase. We stop the integration once $\phi(\hat{\omega})$ reaches its maximum.

Examples of such constructed waveforms are reported in Fig. 2. There, we use the nonspinning BBH waveforms from the SXS-database [33, 34], in particular setup 66 for the equal mass cases and setup 7 for the $q = X_A/X_B = 1.5$ configuration. In order to compare with the BNS configuration with $\chi_{\text{eff}} = +0.123$ we add to the nonspinning NR BBH curve the spin-orbit contributions given

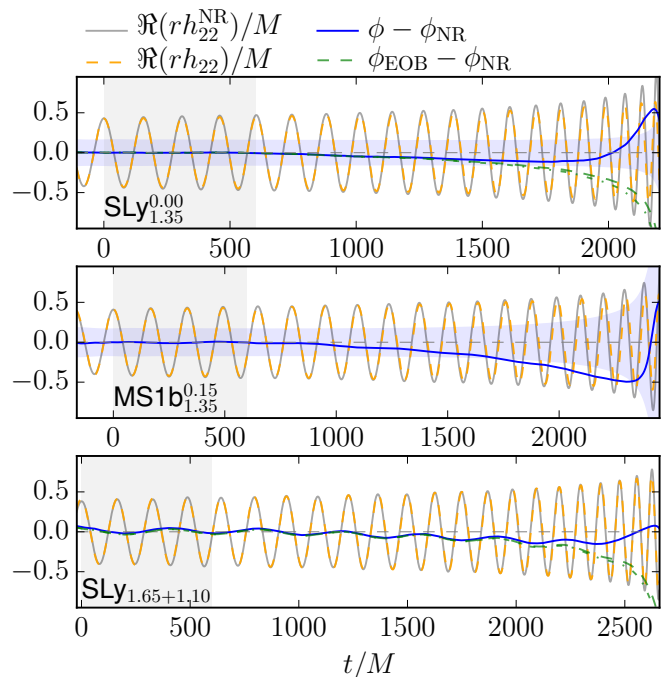


FIG. 2. Comparison of NR simulations with model waveforms obtained following Eq. (3). The panels show the real part of the GW signals (NR data – gray, tidal approximant – orange). We also include the phase between the NR data with respect to our tidal approximant Eq. (5), to Taylor T2 tidal approximant Eq. (4) (cyan), and for some cases to EOB (green dashed [8], green dot dashed [7]). We also indicate the estimated uncertainty of the NR data (blue shaded) and the alignment region (gray shaded). Simulations use the same notation as in Fig. 1 except for the unequal mass case of [14] with $\text{EOS}_{M_A+M_B}$.

in Eq. (417) of [30]. In general a spinning binary black hole baseline should be used.

In most cases our new waveforms are compatible with the NR data within the estimated uncertainties. The proposed tidal approximant remains accurate also for longer waveforms. Phase differences with respect to hybrid tidal EOB-NR waveforms and accumulated over the last 300 orbits before merger are of the order of ~ 1 rad, see [26]. In the nonspinning cases, our results can be directly compared to the tidal EOB waveforms of [7, 8] [see green lines in Fig. 2]; comparable performances are observed in spite of the simplicity of our model. The fit gives a good prediction also for the unequal mass case, although only the leading-order effect of the mass ratio is taken into account, see Eq. (2). Also, while we use NR data up to $\hat{\omega} = 0.17$, the model remains accurate for BNSs with smaller κ_{eff}^T that merge at higher frequencies. Let us stress that the model performances are independent of the BBH baseline, provided the latter is a faithful representation of BBH waveforms.

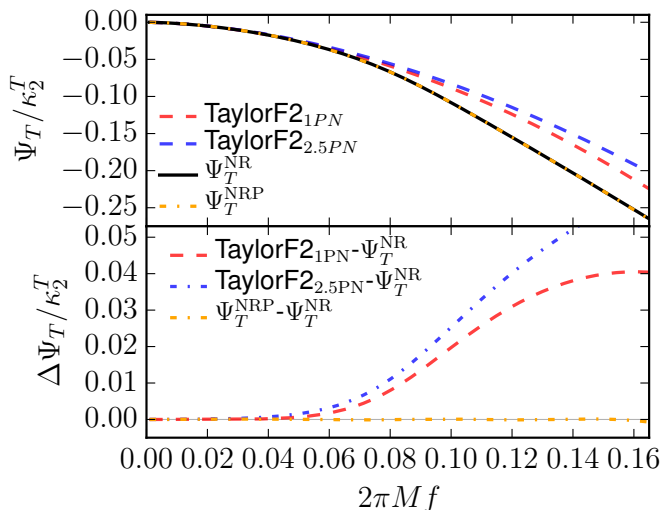


FIG. 3. Frequency-domain tidal approximants. Top panel shows $\Psi_T/\kappa_{\text{eff}}^T$ as given by the TaylorF2_{1PN}, TaylorF2_{2.5PN} [32], Eq. (6), and Eq. (7). Bottom panel: Difference between the frequency-domain representations.

FREQUENCY-DOMAIN TIDAL APPROXIMANT

In the frequency domain, $\tilde{h}(f) = f^{-7/6}\tilde{A}(f)e^{-i\Psi(f)}$. The expression of the tidal phase is computed using the stationary phase approximation (SPA) [32]

$$\frac{d^2\Psi_T^{\text{SPA}}}{d\omega_f^2} = \frac{Q_\omega(\omega_f)}{\omega_f^2}, \quad (6)$$

where ω_f is the Fourier domain circular frequency $\omega_f = 2\pi Mf$, and $Q_\omega(\omega) = d\phi/d\log\omega$. The integration of Eq. (6) with (5) is performed numerically; the constants of integration are fixed by demanding continuity with the TaylorF2_{1PN} in the limit $f \rightarrow 0$. The resulting expression Ψ_T^{NR} can be approximated by a Padé function:

$$\Psi_T^{\text{NRP}} = -\kappa_{\text{eff}}^T \frac{\tilde{c}_{\text{Newt}}}{X_A X_B} x^{5/2} \times \frac{1 + \tilde{n}_1 x + \tilde{n}_{3/2} x^{3/2} + \tilde{n}_2 x^2 + \tilde{n}_{5/2} x^{5/2}}{1 + \tilde{d}_1 x + \tilde{d}_{3/2} x^{3/2}} \quad (7)$$

with $\tilde{c}_{\text{Newt}} = 39/16$ and $\tilde{d}_1 = \tilde{n}_1 - 3115/1248$, the other parameters read: $(\tilde{n}_1, \tilde{n}_{3/2}, \tilde{n}_2, \tilde{n}_{5/2}) = (-17.428, 31.867, -26.414, 62.362)$ and $\tilde{d}_{3/2} = 36.089$.

Figure 3 compares the obtained tidal approximants Ψ_T^{NR} , Ψ_T^{NRP} with the TaylorF2_{1PN} and the 2.5PN approximants given in [32] (TaylorF2_{2.5PN}). Because of the construction of Eq. (7) the low frequency behavior of TaylorF2 is recovered. At higher frequencies PN expressions predict smaller tidal effects than Ψ_T^{NR} . Considering the accuracy of Ψ_T^{NRP} , the Padé fit recovers Ψ_T^{NR} with fractional errors $\lesssim 1\%$.

To further test the performance of the proposed frequency-domain model we compute the unfaithfulness

($\bar{F} = 1 - F$, one minus faithfulness) which is the mismatch for the fixed intrinsic binary parameters with respect to tidal EOB waveforms starting at ~ 25 Hz and hybridized with NR simulations [26]. The unfaithfulness quantifies the loss in the signal-to-noise ratio (squared) due to the inaccuracies in the signal modeling. The typical maximum value used in the GW searches is $\bar{F} \leq 0.03$, which roughly corresponds to $\lesssim 10\%$ loss in the number of events (assuming that they are uniformly distributed).

Figure 4 shows \bar{F} for different approximants and varying the minimum frequency in the overlap interval from $Mf_{\text{min}} \sim [0.0022, 0.04]/2\pi$, i.e. from ~ 27 Hz to the NR regime (~ 480 Hz). Tidal approximants have significant mismatches with respect to BBH ones already for $Mf_{\text{min}} \sim 0.01/2\pi$. The unfaithfulness computed from $Mf_{\text{min}} \sim 0.0022/2\pi$ up to the merger is only weakly dependent on the particular approximant. However, tidal effects become significant at higher frequencies, and if the \bar{F} computations are restricted to higher frequencies significant differences amongst the approximants emerge. Ψ_T^{NRP} has the smallest unfaithfulness. For MS1b_{1.35}^{0.00} (top panel), in particular, the proposed tidal approximant has an unfaithfulness about one order of magnitude smaller than TaylorF2. For SLy_{1.35}^{0.00} (bottom panel) the unfaithfulness is $\bar{F} < 0.03$ for all tidal approximants, indicating that the largest contribution due to tidal effects comes from the strong-field–NR regime.

CONCLUSION

The tidal approximants proposed here can be efficiently used for both GW searches and parameter estimation of BNS events and have shown their use for the interpretation of the recent BNS observation GW170817 [36–39]¹.

For data-analysis applications it is trivial to reparametrize the tidal coupling constant κ_{eff}^T in terms of the mass ratio and (combinations of) the dimensionless tidal parameters that are shown to be optimal for those purposes [18, 19]. The approximant is valid up to the moment of merger frequency defined by NR simulations in [41]. The latter references quantifies the frequency corresponding to the peak of the waveform’s amplitude in term of the tidal polarizability coefficient κ_2^T ; the amplitude’s peak formally marks the end of the chirp signal from BNS. Although our work focused uniquely on the GW phase evolution, tidal corrections to the amplitude could also be added

¹ Details about the implementation in the LSC Algorithm Library Suite and extensive tests of the model can be found in [40].

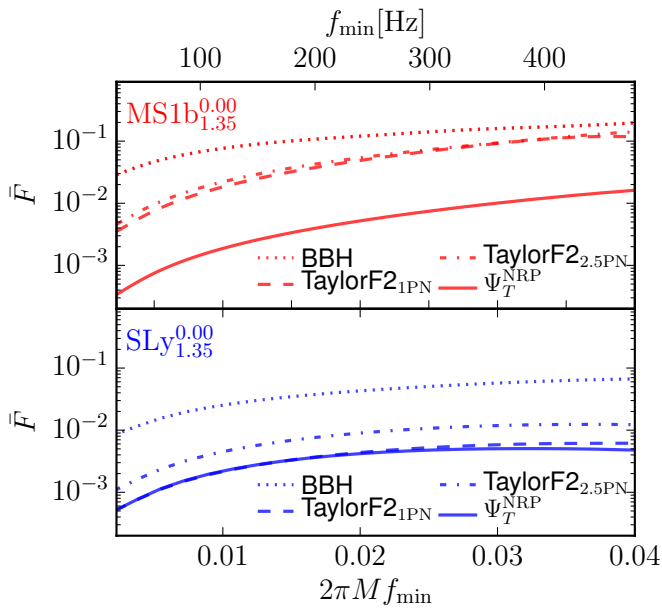


FIG. 4. Unfaithfulness of different approximants with respect to hybridized EOB-NR waveforms for $\text{MS1b}_{1.35}^{0.00}$ (top) and $\text{SLy}_{1.35}^{0.00}$ (bottom). The unfaithfulness is computed within the interval $M[f_{\min}, f_{\max}] \sim [0.0022, 0.04]/2\pi$, i.e. f_{\min} varies between 27 and 480 Hz. f_{\max} is set to the merger frequency of the highest resolved simulation (1398 Hz for $\text{MS1b}_{1.35}^{0.00}$ and 2005 Hz for $\text{SLy}_{1.35}^{0.00}$). As BBH baseline for Ψ_T^{NRP} we use a nonspinning equal-mass EOB waveform [35].

following [32]. Future research will aim at improving the approximants using more NR data and at including precession effects [42, 43]. Our work also proves that high-precision BNS simulations for GW astronomy (similar to those used for the first BBH detections) are now within reach of current technology.

ACKNOWLEDGMENTS

It is a pleasure to thank S. Babak, B. Brügmann, A. Buonanno, R. Cotesta, W. Del Pozzo, T. Hinderer, B. Lackey, K. Kawaguchi, A. Nagar, S. Ossokine, and M. Pürrer for discussions and comments. We thank A. Nagar and T. Hinderer for providing the EOB waveforms. We are grateful to E. Poisson for suggesting the definition of Eq. (2). S.B. acknowledges support by the European Union’s H2020 under ERC Starting Grant, grant agreement no. BinGraSp-714626. W.T. was supported by the National Science Foundation under grant PHY-1305387. Computations were performed on SuperMUC at the LRZ (Munich) under the project number pr48pu, Jureca (Jülich) under the project number HPO21, Stampede (Texas, XSEDE allocation - TG-PHY140019), Marconi (ISCRA-B, under the project number HP10BMAB71), and Marconi (PRACE, pro-

posal number 2016153522).

- [1] B. . Abbott *et al.* (Virgo, LIGO Scientific), *Phys. Rev. Lett.* **116**, 061102 (2016), arXiv:1602.03837 [gr-qc].
- [2] B. P. Abbott *et al.* (Virgo, LIGO Scientific), *Phys. Rev. Lett.* **116**, 241103 (2016), arXiv:1606.04855 [gr-qc].
- [3] B. P. Abbott *et al.* (Virgo, LIGO Scientific), (2016), arXiv:1607.07456 [astro-ph.HE].
- [4] W. Del Pozzo, T. G. F. Li, M. Agathos, C. V. D. Broeck, and S. Vitale, *Phys. Rev. Lett.* **111**, 071101 (2013), arXiv:1307.8338 [gr-qc].
- [5] B. Paczynski, *Astrophys. J.* **308**, L43 (1986).
- [6] N. Tanvir, A. Levan, A. Fruchter, J. Hjorth, K. Wiersema, *et al.*, *Nature* **500**, 547 (2013), arXiv:1306.4971 [astro-ph.HE].
- [7] S. Bernuzzi, A. Nagar, T. Dietrich, and T. Damour, *Phys.Rev.Lett.* **114**, 161103 (2015), arXiv:1412.4553 [gr-qc].
- [8] T. Hinderer *et al.*, (2016), arXiv:1602.00599 [gr-qc].
- [9] A. Buonanno and T. Damour, *Phys. Rev.* **D59**, 084006 (1999), arXiv:gr-qc/9811091.
- [10] T. Damour and A. Nagar, *Phys. Rev.* **D81**, 084016 (2010), arXiv:0911.5041 [gr-qc].
- [11] B. D. Lackey, S. Bernuzzi, C. R. Galley, J. Meidam, and C. Van Den Broeck, (2016), arXiv:1610.04742 [gr-qc].
- [12] S. Bernuzzi, T. Dietrich, W. Tichy, and B. Brügmann, *Phys.Rev.* **D89**, 104021 (2014), arXiv:1311.4443 [gr-qc].
- [13] K. Hotokezaka, K. Kyutoku, H. Okawa, and M. Shibata, *Phys. Rev.* **D91**, 064060 (2015), arXiv:1502.03457 [gr-qc].
- [14] T. Dietrich and T. Hinderer, (2017), arXiv:1702.02053 [gr-qc].
- [15] B. D. Lackey, K. Kyutoku, M. Shibata, P. R. Brady, and J. L. Friedman, *Phys.Rev.* **D89**, 043009 (2014), arXiv:1303.6298 [gr-qc].
- [16] K. Barkett *et al.*, *Phys. Rev.* **D93**, 044064 (2016), arXiv:1509.05782 [gr-qc].
- [17] S. Bernuzzi, A. Nagar, M. Thierfelder, and B. Brügmann, *Phys.Rev.* **D86**, 044030 (2012), arXiv:1205.3403 [gr-qc].
- [18] M. Favata, *Phys.Rev.Lett.* **112**, 101101 (2014), arXiv:1310.8288 [gr-qc].
- [19] L. Wade, J. D. E. Creighton, E. Ochsner, B. D. Lackey, B. F. Farr, *et al.*, (2014), arXiv:1402.5156 [gr-qc].
- [20] S. Khan, S. Husa, M. Hannam, F. Ohme, M. Prrer, X. Jimnez Forteza, and A. Boh, *Phys. Rev.* **D93**, 044007 (2016), arXiv:1508.07253 [gr-qc].
- [21] J. S. Read, B. D. Lackey, B. J. Owen, and J. L. Friedman, *Phys. Rev.* **D79**, 124032 (2009), arXiv:0812.2163 [astro-ph].
- [22] W. Tichy, *Phys. Rev. D* **86**, 064024 (2012), arXiv:1209.5336 [gr-qc].
- [23] M. Thierfelder, S. Bernuzzi, and B. Brügmann, *Phys.Rev.* **D84**, 044012 (2011), arXiv:1104.4751 [gr-qc].
- [24] D. Hilditch, S. Bernuzzi, M. Thierfelder, Z. Cao, W. Tichy, *et al.*, *Phys. Rev.* **D88**, 084057 (2013), arXiv:1212.2901 [gr-qc].
- [25] S. Bernuzzi and T. Dietrich, *Phys. Rev.* **D94**, 064062 (2016), arXiv:1604.07999 [gr-qc].
- [26] T. Dietrich, S. Bernuzzi, and W. Tichy, Supplementary

- material (2017).
- [27] T. Dietrich, N. Moldenhauer, N. K. Johnson-McDaniel, S. Bernuzzi, C. M. Markakis, B. Bruegmann, and W. Tichy, *Phys. Rev.* **D92**, 124007 (2015), arXiv:1507.07100 [gr-qc].
- [28] T. Dietrich, S. Bernuzzi, B. Bruegmann, and W. Tichy (2018) arXiv:1803.07965 [gr-qc].
- [29] T. Dietrich, D. Radice, S. Bernuzzi, F. Zappa, A. Perego, B. Bruegmann, S. V. Chaurasia, R. Dudi, W. Tichy, and M. Ujevic, (2018), arXiv:1806.01625 [gr-qc].
- [30] L. Blanchet, *Living Rev. Relativity* **17**, 2 (2014), arXiv:1310.1528 [gr-qc].
- [31] T. Dietrich, S. Bernuzzi, M. Ujevic, and W. Tichy, *Phys. Rev.* **D95**, 044045 (2017), arXiv:1611.07367 [gr-qc].
- [32] T. Damour, A. Nagar, and L. Villain, *Phys.Rev.* **D85**, 123007 (2012), arXiv:1203.4352 [gr-qc].
- [33] SpEC - Spectral Einstein Code, <http://www.black-holes.org/SpEC.html>.
- [34] A. H. Mroue, M. A. Scheel, B. Szilagyi, H. P. Pfeiffer, M. Boyle, *et al.*, *Phys.Rev.Lett.* **111**, 241104 (2013), arXiv:1304.6077 [gr-qc].
- [35] A. Nagar, T. Damour, C. Reisswig, and D. Pollney, (2015), arXiv:1506.08457 [gr-qc].
- [36] L. Dai, T. Venumadhav, and B. Zackay, (2018), arXiv:1806.08793 [gr-qc].
- [37] B. P. Abbott *et al.* (Virgo, LIGO Scientific), *Phys. Rev. Lett.* **119**, 161101 (2017), arXiv:1710.05832 [gr-qc].
- [38] B. P. Abbott *et al.* (Virgo, LIGO Scientific), (2018), arXiv:1805.11579 [gr-qc].
- [39] B. P. Abbott *et al.* (Virgo, LIGO Scientific), (2018), arXiv:1805.11581 [gr-qc].
- [40] T. Dietrich *et al.*, (2018), arXiv:1804.02235 [gr-qc].
- [41] S. Bernuzzi, A. Nagar, S. Balmelli, T. Dietrich, and M. Ujevic, *Phys.Rev.Lett.* **112**, 201101 (2014), arXiv:1402.6244 [gr-qc].
- [42] K. Chatziioannou, A. Klein, N. Yunes, and N. Cornish, (2013), arXiv:1307.4418 [gr-qc].
- [43] M. Hannam, P. Schmidt, A. Boh, L. Haegel, S. Husa, F. Ohme, G. Pratten, and M. Prerer, *Phys. Rev. Lett.* **113**, 151101 (2014), arXiv:1308.3271 [gr-qc].
- [44] W. Tichy, *Phys.Rev.* **D74**, 084005 (2006), arXiv:gr-qc/0609087 [gr-qc].
- [45] W. Tichy, *Class.Quant.Grav.* **26**, 175018 (2009), arXiv:0908.0620 [gr-qc].
- [46] W. Tichy, *Phys.Rev.* **D80**, 104034 (2009), arXiv:0911.0973 [gr-qc].
- [47] W. Tichy, *Phys.Rev.* **D84**, 024041 (2011), arXiv:1107.1440 [gr-qc].
- [48] K. Kyutoku, M. Shibata, and K. Taniguchi, *Phys. Rev.* **D90**, 064006 (2014), arXiv:1405.6207 [gr-qc].
- [49] B. Brügmann, J. A. Gonzalez, M. Hannam, S. Husa, U. Sperhake, *et al.*, *Phys.Rev.* **D77**, 024027 (2008), arXiv:gr-qc/0610128 [gr-qc].
- [50] T. Dietrich, S. Bernuzzi, M. Ujevic, and B. Bruegmann, *Phys. Rev.* **D91**, 124041 (2015), arXiv:1504.01266 [gr-qc].
- [51] G. Jiang, *J. Comp. Phys.* **126**, 202 (1996).
- [52] A. Suresh, *J. Comp. Phys.* **136**, 83 (1997).
- [53] C. Reisswig and D. Pollney, *Class.Quant.Grav.* **28**, 195015 (2011), arXiv:1006.1632 [gr-qc].
- [54] M. Hannam, S. Husa, U. Sperhake, B. Brügmann, and J. A. González, *Phys. Rev.* **D77**, 044020 (2008), arXiv:0706.1305 [gr-qc].
- [55] C. O. Lousto, H. Nakano, Y. Zlochower, and M. Campanelli, *Phys.Rev.* **D82**, 104057 (2010), arXiv:1008.4360 [gr-qc].
- [56] “LIGO Document T0900288-v3,” Advanced LIGO anticipated sensitivity curves.

SUPPLEMENTARY MATERIAL

Simulations overview

The physical parameters of the BNS configurations and the grid configurations used in the simulations are summarized in Tab. I. The configurations consist of equal mass ($M_A = M_B$) binaries with aligned or anti-aligned spins ($\chi_A = \chi_B$). In total, nine (37) new configurations (simulations) have been performed for the scope of this paper. BNS configurations are indicated by the EOS, the masses (subscript), and the spin (superscript), i.e. $\text{EOS}_{M_A}^{\chi_A}$. We also use non-spinning data from the simulations described in [14] with the notation $(\text{EOS}_{M_A+M_B})$.

Our initial configurations are constructed with the pseudospectral SGRID code [27, 44–46], which makes use of the constant rotational velocity approach [22, 47] to construct constraint solved spinning BNS configurations in hydrodynamical equilibrium. Eccentricity reduced initial data are constructed following [27, 48] by applying an iteration procedure varying the binary’s initial radial velocity and the eccentricity parameter.

Evolutions are performed with the BAM code [23, 25, 49, 50]. We use 7 mesh refinement levels labeled with $l = 0, \dots, 6$ with grid spacing $h_l = h_0/2^l$ for $l > 0$ and number of points per direction n_l . Different grid resolutions named R1, R2, etc. have been employed; the NS diameter is typically covered with $n_6 = 64, 96, 128, 192, 256$ points for respectively R1 to R5 (Table I.) The numerical fluxes for the general relativistic hydrodynamics are computed as in [25] based on a flux-splitting approach with the local Lax-Friedrich flux and after reconstruction of the characteristic fields [51, 52]. This method guarantees clear convergence and a robust error assessment of the numerical simulations, see below.

TABLE I. BNS configurations. The first column defines the name of the configuration with the notation: $\text{EOS}_{M_A}^{\chi_A}$. The subsequent columns describe the corresponding physical properties of the individual stars: the EOS [21], the gravitational mass of the individual stars $M_{A,B}$, the binary mass $M = M_A + M_B$, the binary’s baryonic mass M_b , the stars’ dimensionless spin $\chi_{A,B}$, the effective spin χ_{eff} , the dimensionless quadrupolar tidal coupling constant κ_2^T , the initial dimensionless GW frequency $M\omega_{22}(0)$, the ADM mass $M_{\text{ADM}}(0)$ and angular momentum $J_{\text{ADM}}(0)$ and residual eccentricity estimated from the proper distance, see [27]. The last columns indicate the resolutions employed for BAM’s evolution grid. We use 7 mesh refinement levels $l = 0, \dots, 6$ with refinement ratio 2:1 and grid spacing $h_l = h_0/2^l$ for $l > 0$. We report the number of points per direction in the finest level, n_6 , for all the runs and the grid resolution h_6 in the finest level of the most resolved run. Grid resolutions of other runs can be obtained using $h' = h \cdot n/n'$.

Name	EOS	$M_{A,B}$	M	M_b	$\chi_{A,B}$	χ_{eff}	κ_2^T	$M\omega_{22}(0)$	$M_{\text{ADM}}(0)$	$J_{\text{ADM}}(0)$	$e[10^{-3}]$	n_6	h_6
$\text{MS1b}_{1.35}^{-0.10}$	MS1b	1.3504	2.7008	2.9351	-0.099	-0.082	288.0	0.0357	2.6795	7.4858	1.8	(64,96,128,192)	0.097
$\text{MS1b}_{1.35}^{0.00}$	MS1b	1.3500	2.7000	2.9351	+0.000	+0.000	288.0	0.0357	2.6786	7.8021	1.7	(64,96,128,192)	0.097
$\text{MS1b}_{1.35}^{0.10}$	MS1b	1.3504	2.7008	2.9351	+0.099	+0.082	288.0	0.0357	2.6793	8.1292	1.9	(64,96,128,192)	0.097
$\text{MS1b}_{1.35}^{0.15}$	MS1b	1.3509	2.7018	2.9351	+0.149	+0.123	288.0	0.0357	2.6802	8.3054	1.8	(64,96,128,192)	0.097
$\text{H4}_{1.37}^{0.00}$	H4	1.3717	2.7435	2.9892	+0.000	+0.000	190.0	0.0367	2.7213	8.0052	0.9	(64,96,128,192)	0.083
$\text{H4}_{1.37}^{0.14}$	H4	1.3726	2.7452	2.9892	+0.141	+0.117	190.0	0.0368	2.7229	8.4897	0.4	(64,96,128,192)	0.083
$\text{SLy}_{1.35}^{0.00}$	SLy	1.3500	2.7000	2.9892	+0.000	+0.000	73.5	0.0379	2.6778	7.6860	0.4	(64,96,128,192,256)	0.059
$\text{SLy}_{1.35}^{0.05}$	SLy	1.3502	2.7003	2.9892	+0.052	+0.043	73.5	0.0379	2.6780	7.8588	0.4	(64,96,128,192)	0.078
$\text{SLy}_{1.35}^{0.11}$	SLy	1.3506	2.7012	2.9892	+0.106	+0.088	73.5	0.0379	2.6789	8.0391	0.7	64,96,128,192	0.078

Simulations accuracy

Eccentricity

We construct eccentricity reduced initial data by means of an iterative procedure that monitors and varies the binary’s initial radial velocity and the eccentricity parameter, see Eq. (2.37) and (2.39) of [27]. As an initial guess, quasi-equilibrium configurations in the usual quasi-circular orbit are employed for which residual eccentricities are in the range of $e \sim 10^{-2}$. The steps of the iterative procedure are then, (i) evolve the data for ~ 3 orbits, (ii) measure the eccentricity e , for which we use the proper distance as described in [27], and (iii) re-compute the initial data with adjusted parameters. As an exemplary case, the iteration procedure for the $\text{SLy}_{1.35}^{0.00}$ case is presented in Fig. 5. Target residual eccentricities $e \sim 10^{-3}$ are usually achieved within three iterations [27].

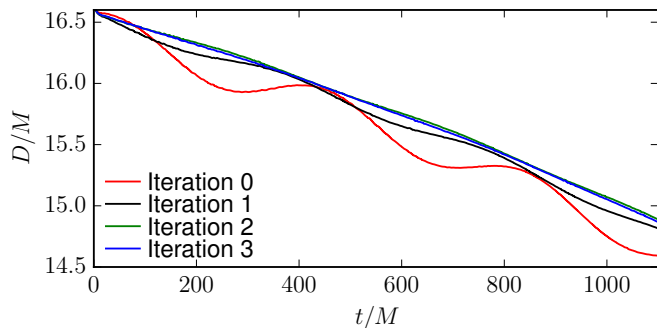


FIG. 5. Proper distance along the connection line between the two NSs centers for $\text{SLy}_{1.35}^{0.00}$.

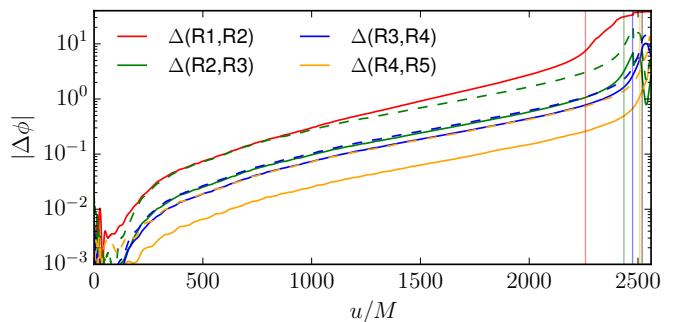


FIG. 6. Phase difference for setup $\text{SLy}_{1.35}^{0.00}$ (solid lines). Dashed lines are rescaled phase differences assuming second order convergence, which is achieved for resolution R2 and above. Straight vertical lines mark the moment of merger, i.e. the peak in the GW amplitude.

Waveform's error-budget

The GW metric multipoles

$$r h_{\ell m}(t) = A_{\ell m}(t) e^{-i\phi_{\ell m}(t)} \quad (8)$$

are constructed from the curvature multipoles using frequency domain integration of Ref. [53]. In this work only the dominant (2,2)-mode is considered and indices are dropped in the following. The retarded time is defined as $u = t - r_*$, where $r_*(M)$ is the tortoise coordinate of the Schwarzschild spacetime of mass M computed from the coordinate (isotropic) radius at which GWs are extracted (see below).

Uncertainties due to truncation errors are estimated following [25]. As an exemplary case we present the phase difference between different resolutions for $\text{SLy}_{1.35}^{0.00}$ in Fig. 6. Second order convergence (dashed lines) is achieved for resolutions R2 and higher. For a better approximation of the waveform we follow the description of [54] and apply a Richardson extrapolation for the phase using the highest three available resolutions for each dataset.

GWs are extracted at finite radii, where we pick $r = 1000$ for our analysis. The numerical error introduced by finite radii extraction of the GW is obtained by comparing finite radii waveforms with second order polynomial extrapolated waveform (similar results are obtained by including next-to-leading order terms, see [25, 55]).

Time-domain approximants

Time-domain fit

To obtain the time-domain fit, we split the interval $\hat{\omega} \in I = [0, 0.17]$ into three different intervals: $I_{T2} = [0, 0.0074]$, $I_{EOB} = [0.0074, 0.04]$, $I_{NR} = [0.04, 0.17]$. In I_{T2} we evaluate Eq. (4) at 10000 equally spaced points. For interval I_{EOB} we compute three tidal EOB waveforms [7] corresponding to the three irrotational runs of Tab. I and with starting frequency $\hat{\omega}(0) = 0.0065$. We compute $\Delta\phi_T/\kappa_2^T$ by taking the difference of $\phi(\hat{\omega})$ for different BNS configurations. From the obtained curves we compute the average and interpolate on an equally spaced grid with a total of 5000 grid points in I_{EOB} . A phase shift is applied to the EOB data by minimizing the phase difference between the T2 and EOB data in the interval $\hat{\omega} \in [0.00715, 0.0765]$. For the interval I_{NR} we compute ϕ_T/κ_2^T by taking the difference between the irrotational NR data [as for the EOB waveforms]; we then take the average of all obtained results, interpolate on an equally spaced grid with 500 grid points, and fix the initial phase by minimizing the phase difference in $[0.04, 0.044]$.

The obtained data on $I = I_{T2} \cup I_{EOB} \cup I_{NR}$ are fitted as a function of x , after factoring out the leading order Newtonian term. The result is given in Eq. (5); the high frequency part of the fit is shown in the bottom panel of Fig. 1.

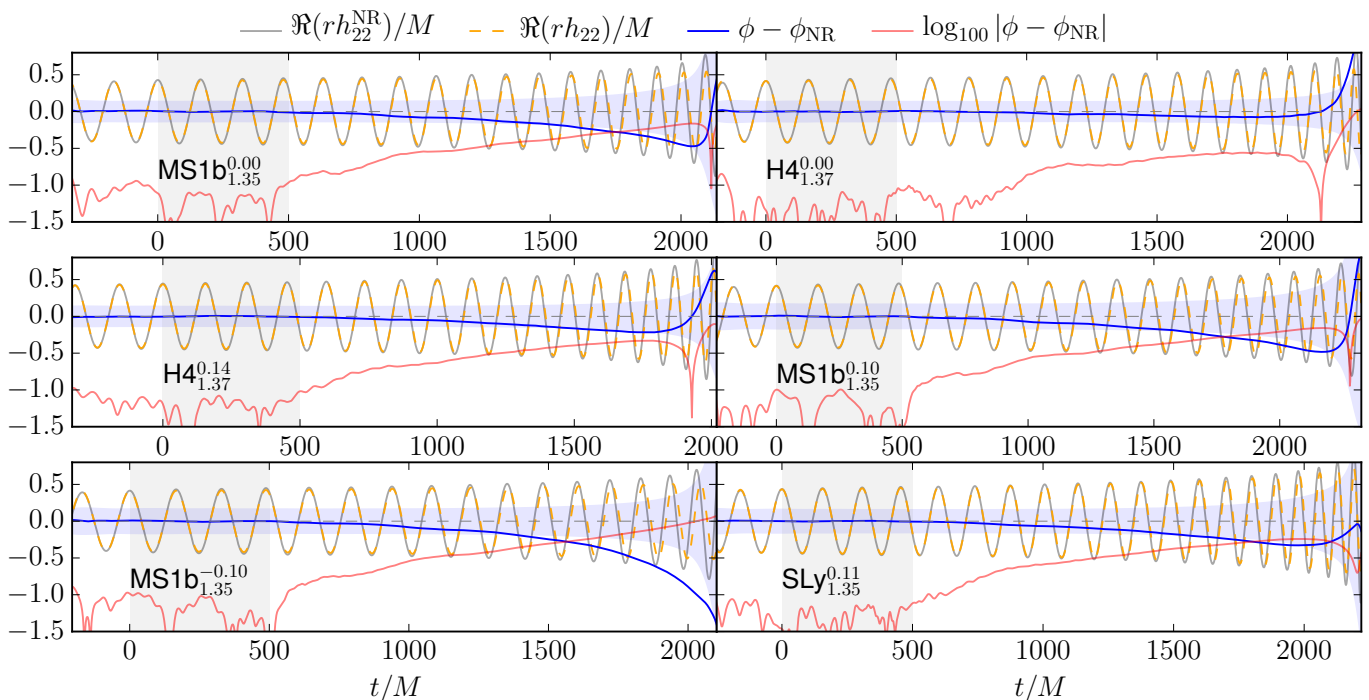


FIG. 7. GWs for different setups, see Tab. I. We compare our waveform model with full NR simulations. For each configuration we show the real part obtained with Eq. (5) (orange) and the real part of the comparison waveform (gray). The dephasing between the model and the comparison waveform $\phi - \phi_{NR}$ is shown blue and $\log_{100} |\phi - \phi_{NR}|$ is shown red. The numerical uncertainty is shown as a blue shaded region and the alignment region as a gray shaded interval.

Waveform comparison

In addition to the exemplary cases in the main text, we further test the performances of the proposed model comparing to

- Waveforms from all the simulations listed in Tab. I [See Fig. 7 for examples].
- Equal and unequal mass NR waveforms of Ref. [14] [see Fig. 8 in which we also include tidal EOB waveforms].
- Hybrid EOB-NR waveforms with a starting frequency of 75 Hz. The hybrid waveforms are constructed by combining tidal EOB waveforms of [7] with the highest resolution irrotational data presented in Tab. I [See Fig. 9 for the results].

We find that our time-domain approximant is robust for a variation of the binary parameters and the waveform length. In particular, spurious effects due to time-domain waveform alignment do not influence significantly our results.

Frequency-domain approximants

The 2.5PN TaylorF2 expression of Damour et al. [32] (DNV) with which we compare reads for equal mass BNSs:

$$\Psi_T^{2.5\text{PN}} = \kappa_2^T \tilde{c}_{\text{Newt}} x^{5/2} (1 + \tilde{c}_1 x + \tilde{c}_{3/2} x^{3/2} + \tilde{c}_2 x^2 + \tilde{c}_{5/2} x^{5/2}), \quad (9)$$

where

$$\tilde{c}_{\text{Newt}} = -\frac{39}{4}, \quad \tilde{c}_1 = \frac{3115}{1248}, \quad \tilde{c}_{3/2} = -\pi, \quad \tilde{c}_2 = \frac{23073805}{3302208} + \frac{20}{81} \bar{\alpha}_2^2 + \frac{20}{351} \beta_2^{22}, \quad \tilde{c}_{5/2} = -\pi \frac{4283}{1092}. \quad (10)$$

For equal masses $\bar{\alpha}_2^2 = 85/14$. The expression above includes tail terms up to 2.5PN order and the 2PN is computed up to an unknown (not yet calculated) coefficient which we set $\beta_2^{22} = 0$.

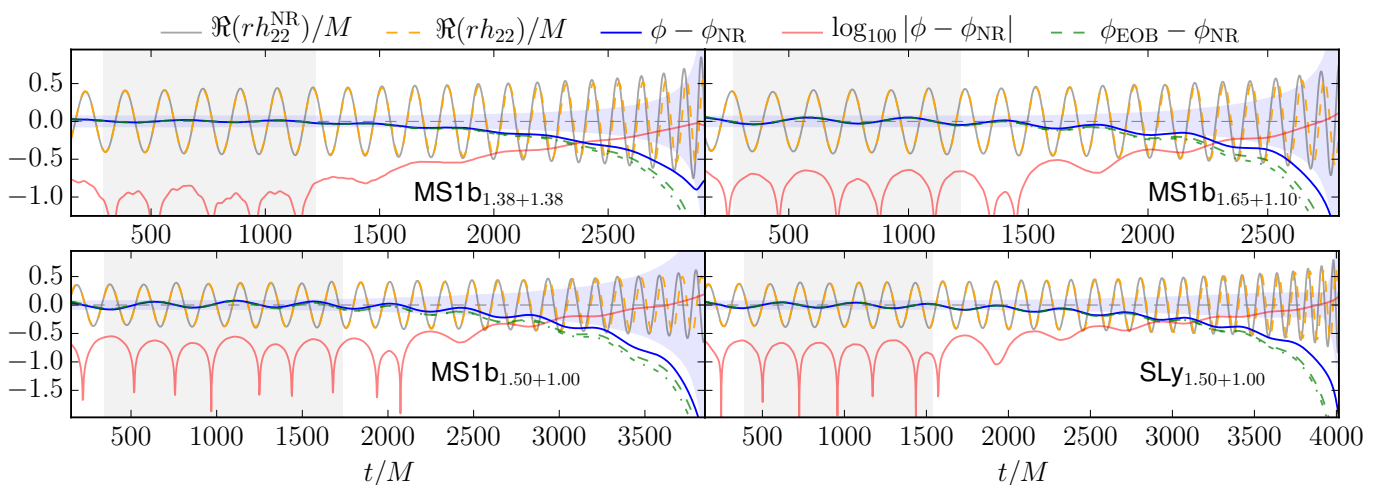


FIG. 8. Comparison of the proposed waveform model with NR simulations of [14]. For each configuration we show the real part obtained with (5) (orange) and the real part of the NR waveform (gray). The dephasing between the model and the NR data $\phi - \phi_{\text{NR}}$ is shown blue and $\log_{10} |\phi - \phi_{\text{NR}}|$ is shown red. We also include the phase between the NR data with respect to the EOB models of [8] (green dashed) and [7] (green dot-dashed). The numerical uncertainty is shown as a blue shaded region and the alignment region as a gray shaded interval. Considered configurations are: an equal mass setups for the MS1b with masses $M_A = M_B = 1.375$ (upper left); an unequal mass setups setup with $M_A = 1.65, M_B = 1.10$ for MS1b (upper right), and unequal mass setups with $M_A = 1.50, M_B = 1.00$ for MS1b (lower left) and SLy (lower right) (bottom row).

To validate the frequency approximant we compute the *mismatch* (or *unfaithfulness*)

$$\bar{F} = 1 - \max_{\phi_c, t_c} \frac{(h_1(\phi_c, t_c) | h_2)}{\sqrt{(h_1 | h_1), (h_2 | h_2)}} \quad (11)$$

with ϕ_c, t_c an arbitrary phase and time shift, and the noise-weighted overlap defined as

$$(h_1, h_2) = 4\Re \int_{f_{\min}}^{f_{\max}} \frac{\tilde{h}_1(f) \tilde{h}_2(f)}{S_n(f)} df . \quad (12)$$

Above, $S_n(f)$ is the one-sided power spectral density of the detector noise, where we use the ZERO_DET_high_P noise curve of [56]. The value of \bar{F} indicates the loss in signal-to-noise ratio (squared) when the waveforms are aligned in time and phase. Template banks are constructed so that the maximum value is $\max(\bar{F}) = 0.03$. Such mismatch corresponds to a maximum loss in event-rate of ~ 0.09 .

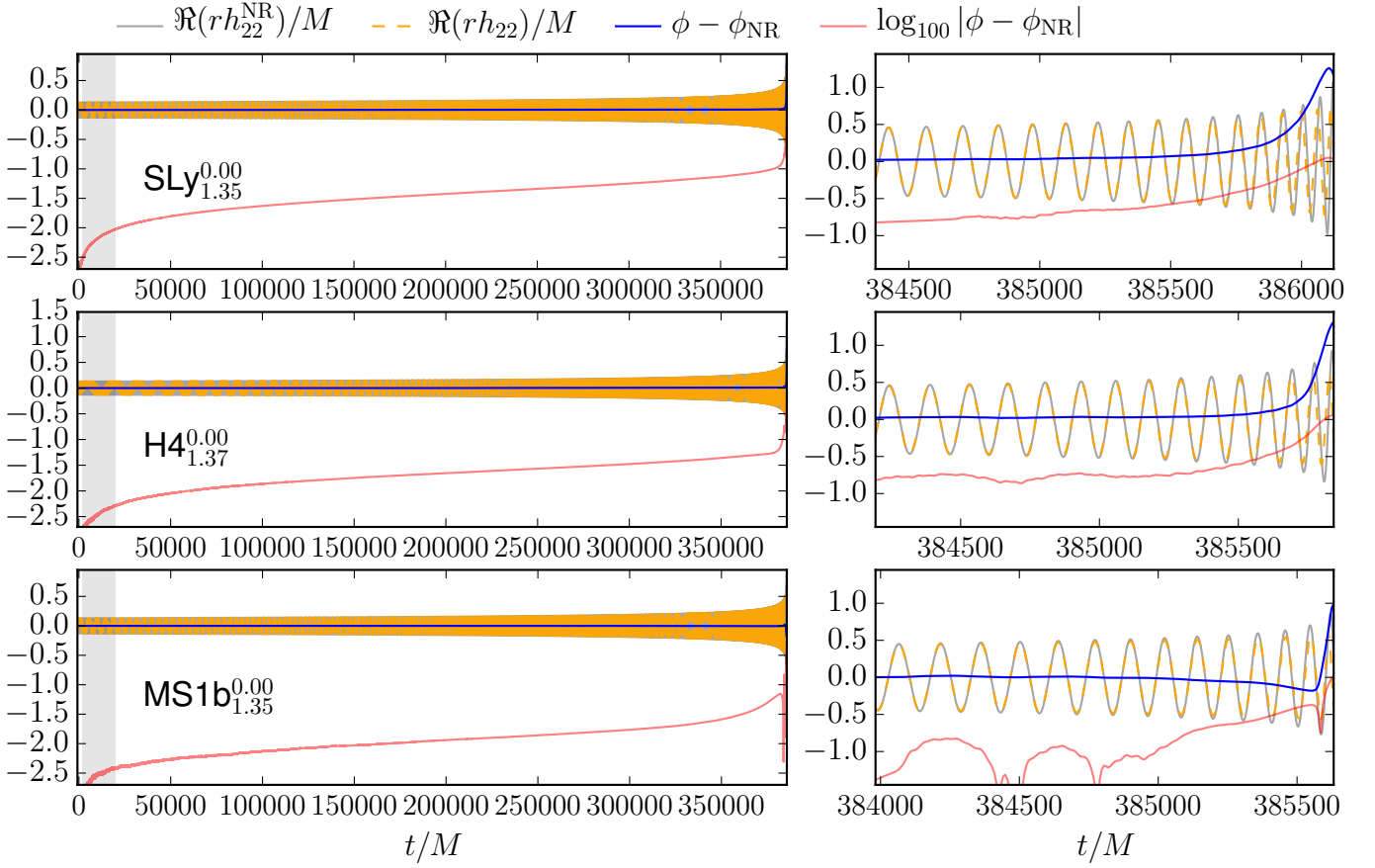


FIG. 9. We compare our waveform model with hybrid NR-tidal EOB waveforms. For each configuration we show the real part obtained with (5) (orange) and the real part of the hybrid waveform (gray). The dephasing between the model and the hybrid $\phi - \phi_{\text{NREOB}}$ is shown blue and $\log_{10} |\phi - \phi_{\text{NREOB}}|$ is shown red. The alignment region is marked as a gray shaded interval. The simulations cover about 300 orbits before the merger.